Available online at www.sciencedirect.com
ScienceDirect
Journal of Computational Physics 227 (2008) 5633–5648
JOURNAL OF COMPUTATIONAL PHYSICS
www.elsevier.com/locate/jcp

Finite-difference modeling of the electroseismic logging in a fluid-saturated porous formation

Wei Guan *, Hengshan Hu

Department of Astronautics and Mechanics, Harbin Institute of Technology, P.O. Box 344, 92 West Dazhi Street, Harbin 150001, China

Received 22 October 2007; received in revised form 3 February 2008; accepted 4 February 2008
Available online 15 February 2008

Abstract

In a fluid-saturated porous medium, an electromagnetic (EM) wavefield induces an acoustic wavefield due to the electrokinetic effect. A potential geophysical application of this effect is electroseismic (ES) logging, in which the converted acoustic wavefield is received in a fluid-filled borehole to evaluate the parameters of the porous formation around the borehole. In this paper, a finite-difference scheme is proposed to model the ES logging responses to a vertical low frequency electric dipole along the borehole axis. The EM field excited by the electric dipole is calculated separately by finite-difference first, and is considered as a distributed exciting source term in a set of extended Biot's equations for the converted acoustic wavefield in the formation. This set of equations is solved by a modified finite-difference time-domain (FDTD) algorithm that allows for the calculation of dynamic permeability so that it is not restricted to low-frequency poroelastic wave problems. The perfectly matched layer (PML) technique without splitting the fields is applied to truncate the computational region. The simulated ES logging waveforms approximately agree with those obtained by the analytical method. The FDTD algorithm applies also to acoustic logging simulation in porous formations.

MSC: 65C20; 65M06; 65N06; 76S05; 76W05; 86A20

Keywords: Finite-difference; FDTD; PML; Porous medium; Electrokinetic; Logging; Acoustic; Electromagnetic

1. Introduction

Electromagnetic (EM) and acoustic wavefields are coupled in a fluid-saturated porous medium due to the electrokinetic effect, which is related to the electric double layer (EDL) at the solid–fluid interface [1]. An EM wave in the medium exerts forces on the excess ions in the EDL, which produces a relative flow of the porous fluid against the solid phase and causes an acoustic wavefield. Conversely, an acoustic wave creates a relative

* Corresponding author. Tel.: +86 13199536607.
E-mail addresses: gwllzh@tom.com (W. Guan), wave_hu@yahoo.com (H. Hu).

0021-9991/$ - see front matter © 2008 Elsevier Inc. All rights reserved.
doi:10.1016/j.jcp.2008.02.001

fluid flow, which carries the ions in the EDL and induces a convection electric current and an EM wavefield. The phenomena of an EM field causing an acoustic wavefield and an acoustic wave inducing an EM wavefield are respectively called electroseismic (ES) conversion and seismoelectric (SE) conversion. Since these electrokinetic phenomena are correlated with the properties of the porous media and the porous fluid flow in the media, potential applications in geophysical exploration and earthquake precursor monitoring were experimentally studied (see e.g. [2–7]).

In the interests of geophysical exploration, SE logging and ES logging methods were put forward and related experiments were conducted by Zhu et al. [8] and Zhu and Toksöz [9,10]. In order to study the characteristics of the electrokinetic logging responses, Hu and Liu [11] and Hu et al. [12] simulated by the analytical method the axisymmetric responses of SE logging and ES logging, respectively, in a fluid-filled borehole within a homogeneous porous formation. If the formation is heterogeneous, numerical techniques, such as finite-difference methods, finite-element methods, must be adopted. In this paper, we propose a finite-difference scheme to model the axisymmetric ES logging responses to a vertical low frequency electric dipole along the borehole axis, which will later be extended to horizontally stratified formations.

The finite-difference time-domain (FDTD) technique first introduced by Yee [13] has been widely used to model EM waves (see e.g. [14–16]) and acoustic waves (see e.g. [17–19]). Nevertheless, it is difficult to be applied to model the coupled EM and acoustic wavefields in a porous formation. Due to the large difference in velocity between EM and acoustic waves, no practical choice of grid size and time step can guarantee both computational efficiency and robustness in the modeling of the coupled wavefields. Fortunately, the influence of the converted acoustic wavefield on the EM field is tiny and can be ignored. Thus the EM field can be decoupled from the converted acoustic field and can be solved separately first. Then taking the known EM field in the formation as a distributed exciting source of the acoustic field and using Biot's dynamic theory of poroelasticity [20,21], the converted acoustic wavefield can be calculated.

The frequency of the electric dipole in the ES logging is several kHz. The wavelength of the EM wave in the formation in such frequency range is in the order of 10^4 m for the media of interest. On the one hand, the region to be discreted for the FDTD method is at least one wavelength multiplied by one wavelength. One the other hand, in order to simulate the EM field in this logging problem, the sampling interval in space must be at least shorter than the borehole radius. This means a huge number of steps in space. It is time consuming and can not be implemented for a single workstation to deal with such a FDTD problem. Fortunately the region of interest in the logging problem is small, less than 10 m from the electric dipole. The EM field in this small region belongs to the near-field because the inequality $r \ll \lambda$ is satisfied, where r is the distance from the source to the field point and λ is the wavelength. In the near-region the field is quasi-stationary, in which the responses from the source to all field points are approximately simultaneous, and at any given time it is governed by Poisson's or Laplace's equations with respect to the electric potential. We first solve for the distribution of the quasi-static EM field in the formation by a finite-difference method. Then calculate the converted acoustic field by modifying the FDTD algorithm of acoustic logging simulation, that is, letting the acoustic source in the borehole in conventional acoustic logging be replaced in ES logging by the distributed EM field-driven source in the formation.

In this paper, we propose an improved FDTD modeling algorithm for acoustic waves in porous media. While previous algorithms (see e.g. [18]) are valid only at low frequencies at which fluid flow in pore space is practically a Poiseuille flow [20], our algorithm is not restricted in frequency by the use in the FDTD implementation of the dynamic permeability defined by Johnson et al. [22].

When applying the FDTD technique to the problem of wave propagation in an infinite medium, absorbing boundary conditions (ABCs) must be employed to eliminate artificial reflections from the boundaries of restricted computation region. Bérenger [23,24] proposed a highly effective perfectly matched layer (PML) as an ABC for EM waves. Then Chew and Liu [25] proved that it can also be applied to acoustic waves. These early schemes require field-splitting in the PML, so that the equations in the PML are different from those in the computational region, which increases the complexity of computation. Roden and Gedney [26] introduced a nonsplitting PML technique for EM waves, in which the equations have the same form in the PML as those in the computational region. Wang and Tang [19] then proposed the nonsplitting PML version for acoustic waves in elastic media. In this paper, we extend their schemes to acoustic and electroseismic wave problems in poroelastic media.

The paper is organized as follows. In Section 2, we interpret Pride's equations that describe the coupling between the EM and acoustic fields. In Section 3, we propose a FDTD algorithm of modeling the acoustic logging responses excited by an acoustic point source on the borehole axis. And we compare the FDTD modeled waveforms with those obtained by an analytical approach called the real-axis integration method [27]. In Section 4, we modify the FDTD algorithm by introducing the electric field into the FDTD formulations of the acoustic field in the formation so that the converted acoustic responses in the ES logging can be calculated out if the electric field is known. To get the distribution of the electric field at any given time in the computational region we formulate in Section 5 a finite-difference method for the static electric equations with respect to the electric potential. The conjugate-gradient iterative technique is employed to solve the equations. In Section 6, we simulate the waveforms of the converted acoustic field in the ES logging and compare the waveforms with those obtained by the analytical method [12].

2. Pride's equations

The governing equations that describe the coupling between the EM and acoustic wavefields in a homogeneous fluid-saturated porous medium were derived by Pride [1], and can be expressed as follows, assuming an $e^{-i\omega t}$ time dependence of all fields.

$$\nabla \times \mathbf{E} = i\omega \mathbf{B}, \tag{1}$$

$$\nabla \times \mathbf{H} = -i\omega \mathbf{D} + \mathbf{J}, \tag{2}$$

$$\mathbf{B} = \mu \mathbf{H}, \tag{3}$$

$$\mathbf{D} = \varepsilon \mathbf{E}, \tag{4}$$

$$\mathbf{J} = \sigma \mathbf{E} + L(-\nabla p + \omega^2 \rho_f \mathbf{u}), \tag{5}$$

$$-i\omega \mathbf{w} = L\mathbf{E} + (-\nabla p + \omega^2 \rho_f \mathbf{u})\kappa/\eta, \tag{6}$$

$$\nabla \cdot \tau = -\omega^2(\rho \mathbf{u} + \rho_f \mathbf{w}), \tag{7}$$

$$\tau = (H - 2G)(\nabla \cdot \mathbf{u})\mathbf{I} + C(\nabla \cdot \mathbf{w})\mathbf{I} + G(\nabla \mathbf{u} + \nabla \mathbf{u}^T), \tag{8}$$

$$-p = C\nabla \cdot \mathbf{u} + M\nabla \cdot \mathbf{w}, \tag{9}$$

where **E**, **D**, **J**, **B** and **H** are the electric field, electric flux density, electric current density, magnetic flux density and magnetic field, respectively, **u** is the displacement of the solid phase, **w** is the relative flow between the fluid and the solid phase, $\boldsymbol{\tau}$ is the bulk stress tensor, **I** is the identity tensor, p is the pore fluid pressure, ε is the permittivity of the formation, μ is the magnetic permeability of the formation and is assumed to equal to the magnetic permeability of vacuum in this paper, ρ_f and η are the density and viscosity of the pore fluid, respectively, ρ is the density of the formation, G is the shear modulus of the formation, H, C and M are porous medium moduli as defined by Biot [21], κ is the dynamic permeability defined by Johnson et al. [22], σ and L are the conductivity and electrokinetic coupling coefficient of the formation, respectively. Electrokinetic coupling between the EM and acoustic wavefields is reflected in (5) and (6) through the terms with the coefficient L.

For the ES conversion of an EM field inducing an acoustic wavefield, the influence of the converted acoustic field on the EM field is weak enough and can be ignored [12,28]. In ES logging, the electric source (such as an electric dipole) which is located in the borehole excites an EM field. The EM field exerts forces on the net ions in the EDL of the formation pore fluid. With the motion of these ions, a fluid flow relative to the pore wall occurs, and a mass transfers through the EDL, resulting in a pressure increase in the region of mass accumulation and a pressure decrease in the region of mass reduction. As a result of this pressure gradient, fluid flows through the central region of the pores where there are no net ions, but in the direction counter to the flow in the EDL. The pressure gradient is maximal when macroscopic Darcy flow through the pores is prohibited. That means the second term on the right hand of (6) reaches its maximum value when $-i\omega \mathbf{w}$ is zero, i.e., $(-\nabla p + \omega^2 \rho_f \mathbf{u})\kappa/\eta = -L\mathbf{E}$. The inertial force $\omega^2 \rho_f \mathbf{u}$ acting on the fluid is added to the pressure gradient term because the fluid motion is measured relative to the solid phase which is a non-inertial reference frame when the electric field is time varying. As such, (5) can be written as

$$\mathbf{J} = \sigma(1 - \eta L^2/\kappa\sigma)\mathbf{E}, \tag{10}$$

where the dimensionless correction term $-\eta L^2/\kappa\sigma$ represents the maximal influence of the acoustic field on the EM field. This term is the same as that in (13) of Haines and Pride [29]. As states by Haines and Pride [29], it typically will satisfy $\eta L^2/\kappa_0\,\sigma<10^{-}5$ (κ_0 is the static Darcy permeability) for the media of interest, which can be safely neglected relative to one. As such, the term $L(-\nabla p+\omega^2\rho_f\mathbf{u})$ in (5) can be neglected. This fact allows the EM field to be completely decoupled from the induced acoustic wavefield so that the EM field is determined by Maxwell's equations. In addition, Hu et al. [12] have simulated the ES logging waveforms by the coupled method (taking into account the influence of the converted acoustic wave on the EM field) as well as the uncoupled method (ignoring this influence). There is no recognizable difference in the waveforms by the two methods.

As can be seen from (6), in ES conversion, the electric field acts as the source of the acoustic field. When the source is absent, (6) becomes

$$-\mathrm{i}\omega\mathbf{w}=(-\nabla p+\omega^2\rho_f\mathbf{u})\kappa/\eta. \tag{11}$$

The combination of (11) and (7)–(9) is Biot's equations [21] for acoustic fields in poroelastic media.

3. FDTD modeling of the acoustic logging

3.1. Discretization of Biot's equations

We adopt the cylindrical coordinates (r,z,θ), with the z-axis being the borehole axis (Fig. 1 shows a schematic diagram of the model). As the fields are symmetric with respect to the z-axis, all the quantities are independent of the θ-coordinate.

First, we rewrite (11) and (7)–(9) in the cylindrical coordinates. In the previous papers on FDTD modeling of acoustic wave propagation in poroelastic media (see e.g. [18]), the viscous force term in Biot's equations was treated as independent of frequency. Such an approximation is valid only when the frequency is so low that the flow in the pore space is a low-frequency viscous flow, i.e., a Poiseuille flow. In this paper, however, the dynamic permeability κ which includes the frequency correction function for the viscous force is directly applied to the FDTD implementation, so that our algorithm is not restricted in frequency. The expression for dynamic permeability κ is given by [1]

$$\kappa(\omega)=\kappa_0\left[\left(1-\frac{4\mathrm{i}\alpha_\infty^2\kappa_0^2\rho_f\omega}{\Lambda^2\phi^2\eta}\right)^{\frac{1}{2}}-\mathrm{i}\frac{\omega\alpha_\infty\rho_f\kappa_0}{\phi\eta}\right]^{-1}, \tag{12}$$

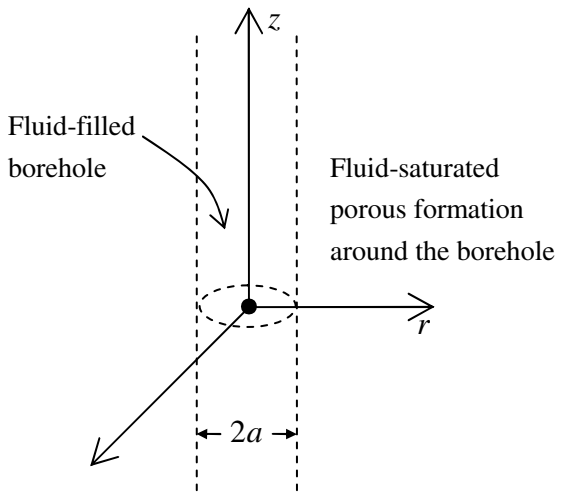

Fig. 1. Schematic diagram of the logging model. The fluid-filled borehole of radius a is surrounded by the fluid-saturated porous formation of infinite extent. The source is located at the origin.

where the term $(1-4\mathrm{i}\alpha_\infty^2\kappa_0^2\rho_\mathrm{f}\omega/\Lambda^2\phi^2\eta)^{\frac{1}{2}}$ dependent on frequency is the frequency correction function for the viscous force term in Biot's equations, α_∞ is the tortuosity, and $\Lambda=\sqrt{m\alpha_\infty\kappa_0/\phi}$ is the weighted volume-to-surface radio defined by Pride [1], where m is a dimensionless number.

Substituting (12) into (11), and setting $D_1=4\alpha_\infty^2\kappa_0^2\rho_\mathrm{f}/\Lambda^2\phi^2\eta$ and $D_2=\alpha_\infty\rho_\mathrm{f}\kappa_0/\phi\eta$, we get

$$\frac{\eta}{\kappa_0}\left(\sqrt{1-\mathrm{i}\omega D_1}-\mathrm{i}\omega D_2\right)\begin{bmatrix}v_{wr}\\ v_{wz}\end{bmatrix}=-\begin{bmatrix}\frac{\partial p}{\partial r}\\ \frac{\partial p}{\partial z}\end{bmatrix}+\mathrm{i}\omega\rho_\mathrm{f}\begin{bmatrix}v_{ur}\\ v_{uz}\end{bmatrix}, \tag{13}$$

where $\mathbf{v}_w=-\mathrm{i}\omega\mathbf{w}$ and $\mathbf{v}_u=-\mathrm{i}\omega\ \mathbf{u}$ are the velocity vectors of the relative flow and the solid phase motion, respectively, v_{wr}, v_{wz}, v_{ur} and v_{uz} are the velocity components. Eqs. (7)–(9) can be rewritten as, respectively,

$$-\mathrm{i}\omega\rho\begin{bmatrix}v_{ur}\\ v_{uz}\end{bmatrix}-\mathrm{i}\omega\rho_\mathrm{f}\begin{bmatrix}v_{wr}\\ v_{wz}\end{bmatrix}=\begin{bmatrix}\frac{\partial}{\partial r}+\frac{1}{r} & -\frac{1}{r} & 0 & \frac{\partial}{\partial z}\\ 0 & 0 & \frac{\partial}{\partial z} & \frac{\partial}{\partial r}+\frac{1}{r}\end{bmatrix}\begin{bmatrix}\tau_{rr}\\ \tau_{\theta\theta}\\ \tau_{zz}\\ \tau_{rz}\end{bmatrix}, \tag{14}$$

$$-\mathrm{i}\omega\begin{bmatrix}\tau_{rr}\\ \tau_{\theta\theta}\\ \tau_{zz}\\ \tau_{rz}\end{bmatrix}=\begin{bmatrix}\frac{H-2G}{r}+H\frac{\partial}{\partial r} & (H-2G)\frac{\partial}{\partial z} & C\left(\frac{1}{r}+\frac{\partial}{\partial r}\right) & C\frac{\partial}{\partial z}\\ \frac{H}{r}+(H-2G)\frac{\partial}{\partial r} & (H-2G)\frac{\partial}{\partial z} & C\left(\frac{1}{r}+\frac{\partial}{\partial r}\right) & C\frac{\partial}{\partial z}\\ (H-2G)\left(\frac{1}{r}+\frac{\partial}{\partial r}\right) & H\frac{\partial}{\partial z} & C\left(\frac{1}{r}+\frac{\partial}{\partial r}\right) & C\frac{\partial}{\partial z}\\ G\frac{\partial}{\partial z} & G\frac{\partial}{\partial r} & 0 & 0\end{bmatrix}\begin{bmatrix}v_{ur}\\ v_{uz}\\ v_{wr}\\ v_{wz}\end{bmatrix}, \tag{15}$$

$$\mathrm{i}\omega p=C\left(\frac{v_{ur}}{r}+\frac{\partial v_{ur}}{\partial r}+\frac{\partial v_{uz}}{\partial z}\right)+M\left(\frac{v_{wr}}{r}+\frac{\partial v_{wr}}{\partial r}+\frac{\partial v_{wz}}{\partial z}\right), \tag{16}$$

where τ_{rr}, $\tau_{\theta\theta}$, τ_{zz} and τ_{rz} are the components of the bulk stress tensor $\boldsymbol{\tau}$.

Next, in order to formulate the equations in the PML, (13)–(16) are modified by stretching the coordinates (see, e.g. [19]). The complex coordinate-stretching variable is chosen as $s_q=1+\Omega_q/\mathrm{i}\omega$, $(q=r,\ z)$ in the frequency domain, where Ω_q is the stretching function with respect to coordinate q. For the PML formulation, the regular coordinate variable q is replaced by the complex coordinate variable $\tilde{q}$, and the spatial derivative $\partial/\partial\tilde{q}$ can be expressed in terms of the complex coordinate-stretching variable as $\partial/\partial\tilde{q}=(1/s_q)\partial/\partial q$. Thus, the r-components of (13) and (14), the first equation in (15) and Eq. (16), for example, can be respectively modified as below, in the complex stretched coordinates,

$$\frac{\eta}{\kappa_0}\left(\sqrt{1-\mathrm{i}\omega D_1}-\mathrm{i}\omega D_2\right)v_{wr}-\mathrm{i}\omega\rho_\mathrm{f}v_{ur}=-\frac{1}{s_r}\frac{\partial p}{\partial r}, \tag{17}$$

$$-\mathrm{i}\omega(\rho v_{ur}+\rho_\mathrm{f}v_{wr})=\left(\frac{1}{s_r}\frac{\partial}{\partial r}+\frac{1}{\tilde{r}}\right)\tau_{rr}-\frac{\tau_{\theta\theta}}{\tilde{r}}+\frac{1}{s_z}\frac{\partial\tau_{rz}}{\partial z}, \tag{18}$$

$$-\mathrm{i}\omega\tau_{rr}=\left(\frac{H-2G}{\tilde{r}}+H\frac{1}{s_r}\frac{\partial}{\partial r}\right)v_{ur}+(H-2G)\frac{1}{s_z}\frac{\partial v_{uz}}{\partial z}+C\left(\frac{1}{\tilde{r}}+\frac{1}{s_r}\frac{\partial}{\partial r}\right)v_{wr}+C\frac{1}{s_z}\frac{\partial v_{wz}}{\partial z}, \tag{19}$$

$$\mathrm{i}\omega p=C\left(\frac{v_{ur}}{\tilde{r}}+\frac{1}{s_r}\frac{\partial v_{ur}}{\partial r}+\frac{1}{s_z}\frac{\partial v_{uz}}{\partial z}\right)+M\left(\frac{v_{wr}}{\tilde{r}}+\frac{1}{s_r}\frac{\partial v_{wr}}{\partial r}+\frac{1}{s_z}\frac{\partial v_{wz}}{\partial z}\right), \tag{20}$$

where $\tilde{r}=\int_0^r s_r(r')\mathrm{d}r'=r(1+\bar{\Omega}_r/\mathrm{i}\omega)$, and $\bar{\Omega}_r=\frac{1}{r}\int_0^r\Omega_r(r')\mathrm{d}r'$.

And then, we transform the equations from the frequency domain to the time domain. Note that the inverse Fourier transform of $s_q^{-1}(q=r,z)$ is

$$F^{-1}\left(\frac{1}{s_q}\right)=F^{-1}\left(1-\frac{\Omega_q}{\Omega_q+\mathrm{i}\omega}\right)=\delta(t)-\Omega_q\mathrm{e}^{-\Omega_q t}, \tag{21}$$

where $\Omega_q\geqslant 0$, and $\delta(t)$ is the Dirac delta function. It follows that

$$F^{-1}\left(\frac{\partial}{\partial\tilde{q}}\right)=[1+\phi_q(t)]\frac{\partial}{\partial q}, \tag{22}$$

where $\phi_q=-\Omega_q\mathrm{e}^{-\Omega_q t}*$ is a convolutional operator. Note also that

$$F^{-1}\left(\frac{1}{\tilde{r}}\right)=\frac{1}{r}F^{-1}\left(1-\frac{\bar{\Omega}_r}{\bar{\Omega}_r+\mathrm{i}\omega}\right)=\frac{1}{r}[\delta(t)-\bar{\Omega}_r\mathrm{e}^{-\bar{\Omega}_r t}]. \tag{23}$$

Using (22) and (23), Eqs. (17)–(20) can be inverse Fourier transformed to the time domain, respectively,

$$\frac{\eta}{\kappa_0}\left(\sqrt{1+D_1\frac{\partial}{\partial t}}+D_2\frac{\partial}{\partial t}\right)v_{wr}+\rho_{\mathrm{f}}\frac{\partial v_{ur}}{\partial t}=-(1+\phi_r)\frac{\partial p}{\partial r}, \tag{24}$$

$$\rho\frac{\partial v_{ur}}{\partial t}+\rho_{\mathrm{f}}\frac{\partial v_{wr}}{\partial t}=\left[(1+\phi_r)\frac{\partial}{\partial r}+\left(\frac{1+\bar{\phi}_r}{r}\right)\right]\tau_{rr}-\left(\frac{1+\bar{\phi}_r}{r}\right)\tau_{\theta\theta}+(1+\phi_z)\frac{\partial\tau_{rz}}{\partial z}, \tag{25}$$

$$\begin{aligned}\frac{\partial\tau_{rr}}{\partial t}=&\left[(H-2G)\left(\frac{1+\bar{\phi}_r}{r}\right)+H(1+\phi_r)\frac{\partial}{\partial r}\right]v_{ur}+(H-2G)(1+\phi_z)\frac{\partial v_{uz}}{\partial z}\\&+C\left[\frac{1+\bar{\phi}_r}{r}+(1+\phi_r)\frac{\partial}{\partial r}\right]v_{wr}+C(1+\phi_z)\frac{\partial v_{wz}}{\partial z},\end{aligned} \tag{26}$$

$$\begin{aligned}-\frac{\partial p}{\partial t}=&C\left[\left(\frac{1+\bar{\phi}_r}{r}\right)v_{ur}+(1+\phi_r)\frac{\partial v_{ur}}{\partial r}+(1+\phi_z)\frac{\partial v_{uz}}{\partial z}\right]\\&+M\left[\left(\frac{1+\bar{\phi}_r}{r}\right)v_{wr}+(1+\phi_r)\frac{\partial v_{wr}}{\partial r}+(1+\phi_z)\frac{\partial v_{wz}}{\partial z}\right],\end{aligned} \tag{27}$$

where $\bar{\phi}_r=-\bar{\Omega}_r\mathrm{e}^{-\bar{\Omega}_r t}*$. Eqs. (24)–(27) are the modified Biot's equations in the PML. When $\Omega_q(q=r,z)$ and $\bar{\Omega}_r$ become zero, these equations automatically reduce to Biot's equations in the computational region.

Now we discrete the velocity and stress fields in Biot's equations by using a staggered finite-difference grid (see e.g. [30]), as shown in Fig. 2. The grid sizes Δr and Δz in the r- and z-directions, respectively, are constant. Because $\sqrt{1+D_1\partial/\partial t}$ in the first term on the left hand of (24) can not be discretized, it is approximated by Taylor series expansion as $\sqrt{1+D_1\partial/\partial t}\approx 1+(D_1/2)\partial/\partial t$. Then, applying the second-order central difference approximations to (24), we get

$$\begin{aligned}&\frac{\eta}{\kappa_0}\left[\frac{1}{2}+\left(\frac{D_1}{2}+D_2\right)\frac{1}{\Delta t}\right]v^{n+1/2}_{wr(j,k+1/2)}+\frac{\rho_{\mathrm{f}}}{\Delta t}v^{n+1/2}_{ur(j,k+1/2)}\\&=\frac{\eta}{\kappa_0}\left[-\frac{1}{2}+\left(\frac{D_1}{2}+D_2\right)\frac{1}{\Delta t}\right]v^{n-1/2}_{wr(j,k+1/2)}+\frac{\rho_{\mathrm{f}}}{\Delta t}v^{n-1/2}_{ur(j,k+1/2)}-\left(\frac{\partial p^n}{\partial r}+P^n_{pr}\right)_{(j,k+1/2)},\end{aligned} \tag{28}$$

where n and $(j,\ k+1/2)$ are the index of time and space steps, respectively, Δt is the time step, and

$$P^n_{pr}=-\Omega_r\int_0^{n\Delta t}\mathrm{e}^{-\Omega_r(n\Delta t-t)}\frac{\partial p(r,t)}{\partial r}\,\mathrm{d}t. \tag{29}$$

Using the trapezoidal integration rule, (29) is approximated as

$$P^n_{pr}=\mathrm{e}^{-\Omega_r\Delta t}P^{n-1}_{pr}-\frac{1}{2}\Omega_r\Delta t\left(\mathrm{e}^{-\Omega_r\Delta t}\frac{\partial p^{n-1}}{\partial r}+\frac{\partial p^n}{\partial r}\right). \tag{30}$$

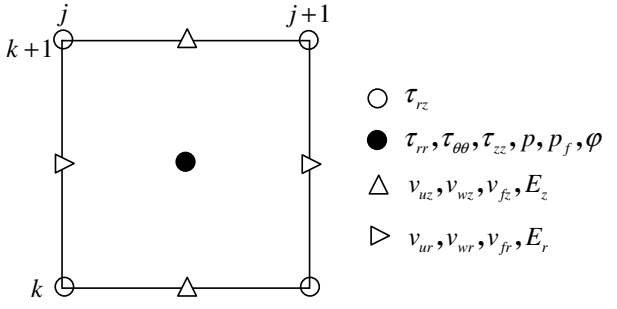

Fig. 2. The FDTD grid in cylindrical coordinates. p_{f}, $v_{\mathrm{f}r}$ and $v_{\mathrm{f}z}$ are the acoustic wave field quantities in the borehole. φ, E_r and E_z represent the electric field quantities. The other quantities denote the acoustic wave field in the formation.

Similar to the processing of (24), Eq. (25) can be discretized as

$$\rho v_{ur(j,k+1/2)}^{n+1/2} + \rho_{\mathrm{f}} v_{wr(j,k+1/2)}^{n+1/2} = \rho v_{ur(j,k+1/2)}^{n-1/2} + \rho_{\mathrm{f}} v_{wr(j,k+1/2)}^{n-1/2} + \Delta t\left[\left(\frac{\partial \tau_{rr}^{n}}{\partial r} + P_{rrr}^{n}\right) + \left(\frac{\tau_{rr}^{n} - \tau_{\theta\theta}^{n} + Q_{r\_\theta r}^{n}}{r}\right) + \left(\frac{\partial \tau_{rz}^{n}}{\partial z} + P_{rzz}^{n}\right)\right]_{(j,k+1/2)}, \tag{31}$$

where

$$P_{rrr}^{n} = \mathrm{e}^{-\Omega_r \Delta t} P_{rrr}^{n-1} - \frac{1}{2}\Omega_r \Delta t\left(\mathrm{e}^{-\Omega_r \Delta t}\frac{\partial \tau_{rr}^{n-1}}{\partial r} + \frac{\partial \tau_{rr}^{n}}{\partial r}\right), \tag{32}$$

$$Q_{r\_\theta r}^{n} = \mathrm{e}^{-\bar{\Omega}_r \Delta t} Q_{r\_\theta r}^{n-1} - \frac{1}{2}\bar{\Omega}_r \Delta t\left[\mathrm{e}^{-\bar{\Omega}_r \Delta t}\left(\tau_{rr}^{n-1} - \tau_{\theta\theta}^{n-1}\right) + \tau_{rr}^{n} - \tau_{\theta\theta}^{n}\right], \tag{33}$$

$$P_{rzz}^{n} = \mathrm{e}^{-\Omega_z \Delta t} P_{rzz}^{n-1} - \frac{1}{2}\Omega_z \Delta t\left(\mathrm{e}^{-\Omega_z \Delta t}\frac{\partial \tau_{rz}^{n-1}}{\partial z} + \frac{\partial \tau_{rz}^{n}}{\partial z}\right). \tag{34}$$

To solve (28) and (31), we can derive $v_{ur(j,k+1/2)}^{n+1/2}$ and $v_{wr(j,k+1/2)}^{n+1/2}$. The other field quantities $v_{uz(j+1/2,k)}^{n+1/2}$, $v_{wz(j+1/2,k)}^{n+1/2}$, $\tau_{rr(j+1/2,k+1/2)}^{n+1}$, $\tau_{\theta\theta(j+1/2,k+1/2)}^{n+1}$, $\tau_{zz(j+1/2,k+1/2)}^{n+1}$, $\tau_{rz(j,k)}^{n+1}$ and $p_{(j+1/2,k+1/2)}^{n+1}$ can also be derived from the other equations in (13)–(16) by the similar discretization process mentioned above.

All the space derivatives of the FDTD implementation are approximated by the second-order central difference. For example, the space derivative in (28) is approximated as $\partial p_{(j,k+1/2)}^{n}/\partial r = (p_{(j+1/2,k+1/2)}^{n} - p_{(j-1/2,k+1/2)}^{n})/\Delta r$.

3.2. Discretization of the equations in the borehole

The first-order equations of the acoustic wave in the fluid-filled borehole can be expressed as [17]

$$\rho_{\mathrm{b}} \frac{\partial \mathbf{v}_{\mathrm{f}}}{\partial t} = -\nabla p_{\mathrm{f}}, \tag{35}$$

$$\frac{\partial p_{\mathrm{f}}}{\partial t} = -\rho_{\mathrm{b}} c_{\mathrm{bm}}^2 \nabla \cdot \mathbf{v}_{\mathrm{f}} + G(r,z,t), \tag{36}$$

where p_{f} is the borehole fluid pressure, $\mathbf{v}_{\mathrm{f}}$ and ρ_{b} are the velocity vector and the density of the borehole fluid, respectively, c_{bm} is the sound speed in the borehole fluid, and $G(r, z, t)$ is the function determined by the source, which becomes zero for source-free grids.

Similar to the processes mentioned in Section 3.1, and noting that Ω_r and $\bar{\Omega}_r$ become zero due to the absence of the r-direction PML in the borehole, the acoustic wave equations for source-free grids are discretized as (Fig. 2 shows the grid for the field quantities in the borehole)

$$v_{\mathrm{fr}(j,k+1/2)}^{n+1/2} = v_{\mathrm{fr}(j,k+1/2)}^{n-1/2} - \frac{\Delta t}{\rho_{\mathrm{b}}}\frac{\partial p_{\mathrm{f}(j,k+1/2)}^{n}}{\partial r}, \tag{37}$$

$$v_{\mathrm{fz}(j+1/2,k)}^{n+1/2} = v_{\mathrm{fz}(j+1/2,k)}^{n-1/2} - \frac{\Delta t}{\rho_{\mathrm{b}}}\left(\frac{\partial p_{\mathrm{f}}^{n}}{\partial z} + P_{pfz}^{n}\right)_{(j+1/2,k)}, \tag{38}$$

$$p_{\mathrm{f}(j+1/2,k+1/2)}^{n+1} = p_{\mathrm{f}(j+1/2,k+1/2)}^{n} - \rho_{\mathrm{b}} c_{\mathrm{bm}}^2 \Delta t\left[\frac{\partial v_{\mathrm{fr}}^{n+1/2}}{\partial r} + \frac{v_{\mathrm{fr}}^{n+1/2}}{r} + \left(\frac{\partial v_{\mathrm{fz}}^{n+1/2}}{\partial z} + P_{\mathrm{vfz}}^{n+1/2}\right)\right]_{(j+1/2,k+1/2)}, \tag{39}$$

where v_{fr} and v_{fz} are the components of the velocity vector $\mathbf{v}_{\mathrm{f}}$, and

$$P_{\mathrm{pfz}}^{n} = \mathrm{e}^{-\Omega_z \Delta t} P_{\mathrm{vfz}}^{n-1} - \frac{1}{2}\Omega_z \Delta t\left(\mathrm{e}^{-\Omega_z \Delta t}\frac{\partial p_{\mathrm{f}}^{n-1}}{\partial z} + \frac{\partial p_{\mathrm{f}}^{n}}{\partial z}\right), \tag{40}$$

$$P_{\mathrm{vfz}}^{n+1/2} = \mathrm{e}^{-\Omega_z \Delta t} P_{\mathrm{vfz}}^{n-1/2} - \frac{1}{2}\Omega_z \Delta t\left(\mathrm{e}^{-\Omega_z \Delta t}\frac{\partial v_{\mathrm{fz}}^{n-1/2}}{\partial z} + \frac{\partial v_{\mathrm{fz}}^{n+1/2}}{\partial z}\right). \tag{41}$$

The excitation source in the acoustic logging is a point source as described by Tsang and Rader [31], with the peak pressure being 100 Pa at a location of 0.01 m away from the source. This source is introduced by letting $G(r,z,t) = 4\pi c_{\mathrm{bm}}^2 \delta(r,z) S(t)$ in (36), where $\delta(r,z)$ is the delta function, $S(t) = \int_0^t s(t')\mathrm{d}t'$, and the source pulse function $s(t)$ used in this paper is

$$s(t) = \begin{cases} \frac{1}{2}\left[1 + \cos\frac{2\pi}{T_c}\left(t - \frac{T_c}{2}\right)\right]\cos 2\pi f_0\left(t - \frac{T_c}{2}\right), & 0 \leqslant t \leqslant T_c \\ 0, \quad t < 0 \quad \text{or} \quad t > T_c \end{cases}, \tag{42}$$

where the center frequency $f_0 = 6$ kHz and the pulse width $T_c = 0.5$ ms. Eq. (36) for the source grid can be discretized by the volume integral method. Using the generalized Gauss formula, the volume integral of (36) is expressed as (see Fig. 3)

$$\int\int\int_{\Omega} \frac{\partial p_{\mathrm{f}}}{\partial t}\mathrm{d}V = -\rho_{\mathrm{b}} c_{\mathrm{bm}}^2 \oint\!\!\oint_{\Sigma} \mathbf{v}_{\mathrm{f}} \cdot \mathrm{d}\mathbf{s} + 4\pi c_{\mathrm{bm}}^2 S(t) \int\int\int_{\Omega} \delta(r,z)\mathrm{d}V, \tag{43}$$

where Ω and Σ denote the volume and the surface area of the cylindrical body shown in Fig. 3. Applying the integral mean value theorem to (43), yields

$$p_{\mathrm{f}(1/2,1/2)}^{n+1} = p_{\mathrm{f}(1/2,1/2)}^{n} + \frac{c_{\mathrm{bm}}^2 \Delta t}{\Delta z}\left[-\rho_{\mathrm{b}}\left(v_{\mathrm{f}z(1/2,1)}^{n+1/2} - v_{\mathrm{f}z(1/2,0)}^{n+1/2} + 2\frac{\Delta z}{\Delta r} v_{\mathrm{f}r(1,1/2)}^{n+1/2}\right) + \frac{4}{(\Delta r)^2} F^{n+1/2}\right]. \tag{44}$$

3.3. The quantities at the borehole wall

For EM wave problems, the method of averaging the adjacent medium parameters can be used to calculate the field quantities at the boundary (see e.g. [14]). However, it can not be applied to borehole acoustic-field problems because the governing equations in the formation are different from those in the borehole. Our method is presented as below.

At the borehole wall ($j = r_a$), the quantity $v_{\mathrm{f}r(r_a,k+1/2)}^{n+1/2}$ can not be discretized directly according to (37), because the space derivative $\partial/\partial r$ in (37) breaks at the medium interface. Using the approximation $\partial p_{\mathrm{f}(r_a,k+1/2)}^{n}/\partial r \approx \partial p_{\mathrm{f}(r_a-1/4,k+1/2)}^{n}/\partial r$ in (37) yields

$$v_{\mathrm{f}r(r_a,k+1/2)}^{n+1/2} = v_{\mathrm{f}r(r_a,k+1/2)}^{n-1/2} - \frac{\Delta t}{\rho_{\mathrm{b}}}\frac{\partial p_{\mathrm{f}(r_a-1/4,k+1/2)}^{n}}{\partial r}, \tag{45}$$

where

$$\frac{\partial p_{\mathrm{f}(r_a-1/4,k+1/2)}^{n}}{\partial r} = \frac{2(p_{\mathrm{f}(r_a,k+1/2)}^{n} - p_{\mathrm{f}(r_a-1/2,k+1/2)}^{n})}{\Delta r}. \tag{46}$$

Similarly, the quantities $v_{ur(r_a,k+1/2)}^{n+1/2}$ and $v_{wr(r_a,k+1/2)}^{n+1/2}$ at the borehole wall can not be obtained from (28) and (31). Introducing the approximation $\partial p_{(r_a,k+1/2)}^{n}/\partial r \approx \partial p_{(r_a+1/4,k+1/2)}^{n}/\partial r$ to (28) and the approximations

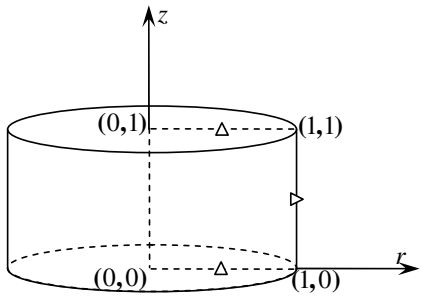

Fig. 3. Schematic diagram of the volume integral region of the source-grid.

$\partial\tau^n_{rr(r_a,k+1/2)}/\partial r \approx \partial\tau^n_{rr(r_a+1/4,k+1/2)}/\partial r$ and $\tau^n_{\theta\theta(r_a,k+1/2)} \approx (3\tau^n_{\theta\theta(r_a+1/2,k+1/2)} - \tau^n_{\theta\theta(r_a+3/2,k+1/2)})/2$ to (31), and using the fact that the variables P^n_{pr} in (28) and P^n_{rrr} and $Q^n_{r\_\theta r}$ in (31) are zero at the borehole wall, we have

$$\frac{\eta}{\kappa_0}\left[\frac{1}{2}+\left(\frac{D_1}{2}+D_2\right)\frac{1}{\Delta t}\right]v^{n+1/2}_{wr(r_a,k+1/2)}+\frac{\rho_f}{\Delta t}v^{n+1/2}_{ur(r_a,k+1/2)}$$
$$=\frac{\eta}{\kappa_0}\left[-\frac{1}{2}+\left(\frac{D_1}{2}+D_2\right)\frac{1}{\Delta t}\right]v^{n-1/2}_{wr(r_a,k+1/2)}+\frac{\rho_f}{\Delta t}v^{n-1/2}_{ur(r_a,k+1/2)}-\frac{\partial p^n_{(r_a+1/4,k+1/2)}}{\partial r}, \tag{47}$$

$$\rho v^{n+1/2}_{ur(r_a,k+1/2)}+\rho_f v^{n+1/2}_{wr(r_a,k+1/2)}$$
$$=\rho v^{n-1/2}_{ur(r_a,k+1/2)}+\rho_f v^{n-1/2}_{wr(r_a,k+1/2)}+\Delta t\left[\frac{\partial\tau^n_{rr(r_a+1/4,k+1/2)}}{\partial r}-\frac{1}{r}\left(\frac{3}{2}\tau^n_{\theta\theta(r_a+1/2,k+1/2)}-\frac{1}{2}\tau^n_{\theta\theta(r_a+3/2,k+1/2)}\right)\right.$$
$$\left.+\left(\frac{\tau^n_{rr}}{r}+\frac{\partial\tau^n_{rz}}{\partial z}+P^n_{rzz}\right)_{(r_a,k+1/2)}\right], \tag{48}$$

where

$$\frac{\partial p^n_{(r_a+1/4,k+1/2)}}{\partial r}=\frac{2\left(p^n_{(r_a+1/2,k+1/2)}-p^n_{(r_a,k+1/2)}\right)}{\Delta r}, \tag{49}$$

$$\frac{\partial\tau^n_{rr(r_a+1/4,k+1/2)}}{\partial r}=\frac{2\left(\tau^n_{rr(r_a+1/2,k+1/2)}-\tau^n_{rr(r_a,k+1/2)}\right)}{\Delta r} \tag{50}$$

The acoustic fields in the borehole and formation obey the boundary conditions at the borehole wall:

$$v^{n+1/2}_{fr(r_a,k+1/2)}=v^{n+1/2}_{ur(r_a,k+1/2)}+v^{n+1/2}_{wr(r_a,k+1/2)}, \tag{51}$$

$$p^n_{f(r_a,k+1/2)}=p^n_{(r_a,k+1/2)}, \tag{52}$$

$$-p^n_{f(r_a,k+1/2)}=\tau^n_{rr(r_a,k+1/2)}, \tag{53}$$

$$0=\tau^n_{rz(r_a,k)}. \tag{54}$$

From (54), we derive that the term $(\partial\tau^n_{rz}/\partial z+P^n_{rzz})_{(r_a,k+1/2)}$ in (48) is zero. When substituting (52) and (53) into (47) and (48), respectively, there remain four unknown field quantities in Eqs. (45), (47), (48) and (51). By solving these equations, we derive the field quantities at the borehole wall, i.e., $v^{n+1/2}_{fr(r_a,k+1/2)}$, $v^{n+1/2}_{ur(r_a,k+1/2)}$ and $v^{n+1/2}_{wr(r_a,k+1/2)}$.

3.4. Numerical modeling of acoustic logging

In this section, we check the FDTD implementation for the acoustic logging modeling proposed in Sections 3.1–3.3. We compare the simulated waveforms with those obtained by the real-axis integration method [27] when the porous formation around the borehole is homogeneous.

Parameters of the borehole and the formation for modeling the acoustic logging and the ES logging later in this paper are listed in Table 1. The formation has a compressional velocity of 3975 m/s and a shear velocity of 2455 m/s. We set the grid sizes $\Delta r=\Delta z=0.0125$ m according to the formula $\Delta r=V_{\min}/10f_{\max}$ in [32], where $V_{\min}$ is the minimum body wave velocity ($V_{\min}=1500$ m/s, i.e., the acoustic wave speed in the borehole fluid used in this paper), and $f_{\max}$ is the maximum source frequency (we set $f_{\max}=2f_0$). The time step is chosen as $\Delta t=2\times10^{-3}$ ms, in terms of the Courant stability $\Delta t<\Delta r/\sqrt{2}V_{\max}$, where $V_{\max}$ is the maximum wave velocity ($V_{\max}=3975$ m/s, i.e., the compressional wave velocity of the formation used in this paper). There are 200 and 400 cells in the r- and z-directions of the computational region, respectively. The PML contains 60 cells in all sides outside the computational region. We choose the stretching function $\Omega_q(q)=-V_{\max}(a\gamma+b\gamma^2)\ln\alpha/T$, $(q=r,z)$ as in [19], where $\gamma=q/T$, T is the width of the PML, $\alpha=10^{-6}$ is a predefined level of wave absorption, and the coefficients $a=0.25$ and $b=0.75$ are used.

Fig. 4 shows the FDTD modeled pressure responses of the acoustic logging at different locations along the borehole axis. Note that the results are normalized with respect to the peak value of the response at the

Table 1
Input parameters of the formation and the borehole. The relationships between ϕ and K_b and G_b are assumed to obey the experimental results of [33]

Parameter	Property	Value
a	Borehole radius (m)	0.1
ϕ	Porosity (%)	20
κ_0	Static Darcy permeability (Darcy)	1
K_b	Frame bulk modulus (GPa)	14.39
G_b	Frame shear modulus (GPa)	13.99
K_f	Solid bulk modulus (GPa)	35.70
K_f	Pore fluid bulk modulus (GPa)	2.25
ρ_s	Solid density (kg/m^3)	2650
ρ_f, ρ_b	Pore fluid density, borehole fluid density (kg/m^3)	1000
C_f, C_b	Pore fluid salinity, borehole fluid salinity (mol/L)	0.01
σ_f, σ_b	Pore fluid conductivity, borehole fluid conductivity(S/m)	9.28×10^{-2}
η	Pore fluid viscosity (Pa s)	10^{-3}
V_{bm}	Acoustic velocity in borehole fluid (m/s)	1500
α_∞	Tortuosity	3

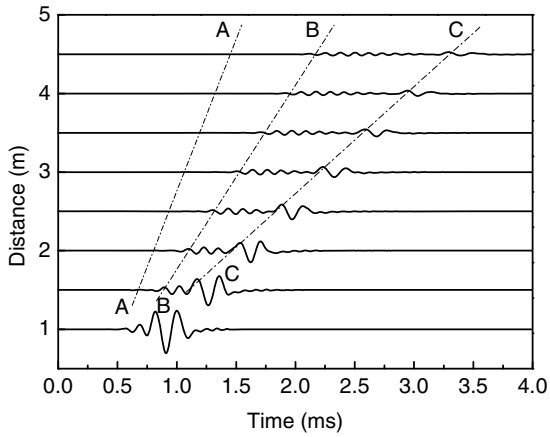

Fig. 4. Waveforms of the pressure in acoustic logging received at different locations along the borehole axis.

location of the receiver-to-source distance $z = 1$ m. There are three wave groups in the waveforms (shown by lines A–A, B–B and C–C in Fig. 4): compressional wave group, shear and pseudo-Rayleigh wave group, and Stoneley wave group. Shown in Fig. 5 are the comparisons between the FDTD and the real-axis integration methods of pressure responses in the acoustic logging. It is seen that the FDTD modeled waveforms are of the same amplitudes as those from real-axis integration method, and they are almost in phase apart from the Stoneley wave group, for which a small deviation in phase occurred between the two methods.

4. Modified FDTD algorithm for ES logging

The acoustic field in acoustic logging is excited by the acoustic source in the borehole; in ES logging, however, it is induced from the EM field in the porous formation due to the electrokinetic effect. This converted acoustic field is governed by the set of extended Biot's equations composed of (6)–(9), which reduces to conventional Biot's equations when the term $L\mathbf{E}$ in (6) becomes zero. Thus in ES logging the excitation source of the converted acoustic field is the distributed electric field in the formation.

In order to discrete (6), we rewrite it as

$$\mathbf{v}_w = \mathbf{v}_{w\_A} + \mathbf{v}_{w\_EM}, \tag{55}$$

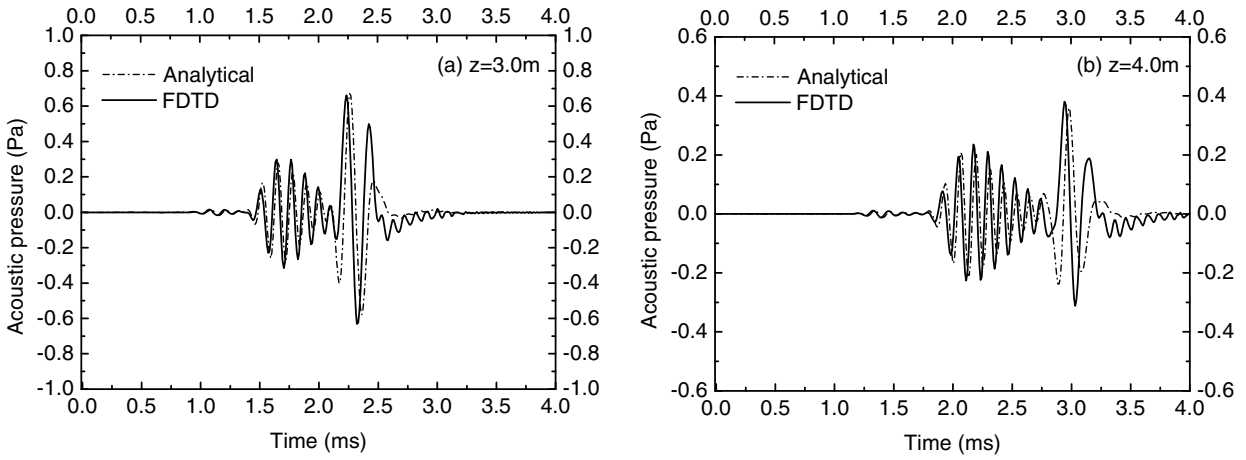

Fig. 5. Comparisons between the FDTD and the real-axis integration methods of the waveforms of pressure in acoustic logging. (a) $z = 3.0$ m and (b) $z = 4.0$ m.

where $\mathbf{v}_{w\_A} = (-\nabla p + \omega^2 \rho_f \mathbf{u})\kappa/\eta$ and $\mathbf{v}_{w\_EM} = L\mathbf{E}$ represent the relative flow velocities that concern with the acoustic field and the electric field, respectively. The quantity $\mathbf{v}_{w\_A}$ can be discretized from (11) using the FDTD implementation of the acoustic logging simulation proposed in this paper. Now, we only need to discrete the quantity $\mathbf{v}_{w\_EM}$.

The electrokinetic coupling coefficient L is given by [1]

$$L = L_0 \left[1 - i\omega \frac{\rho_f \Lambda^2}{4\eta} \left(1 - 2\frac{\tilde{d}}{\Lambda} \right)^2 \left(1 - i^{\frac{3}{2}} \frac{\tilde{d}}{\delta} \right)^2 \right]^{-\frac{1}{2}}, \tag{56}$$

where $L_0 = -(\phi \varepsilon_f \varsigma / \alpha_\infty \eta)(1 - 2\alpha_\infty \tilde{d}/\Lambda)$ is the low-frequency electrokinetic coupling coefficient, and for the formation parameters used in this paper L can be approximated to L_0 when the frequency is less than 1 kHz, ε_f is the permittivity of the fluid in the porous formation, ς is called the zeta potential which is the electric potential at the shear plane, which separates the two layers, i.e., the adsorbed layer and the diffuse layer in the EDL, δ is the viscous skin depth, $\tilde{d}$ is the length defined by Pride [1] that is equal to or less than the Debye length. According to [1], the assumption $\tilde{d}/\delta \ll 1$ can always be satisfied in common rocks, if the frequency is less than 10^3 kHz. Thus (56) for the expression of L can be approximated as

$$L = L_0 \left[1 - i\omega \frac{\rho_f \Lambda^2}{4\eta} \left(1 - 2\frac{\tilde{d}}{\Lambda} \right)^2 \right]^{-\frac{1}{2}}. \tag{57}$$

By substituting (57) into $\mathbf{v}_{w\_EM} = L\mathbf{E}$, and setting $D_3 = \rho_f \Lambda^2 (1 - 2\tilde{d}/\Lambda)^2 / 4\eta$, we have $v_{w\_EM}\sqrt{1 - i\omega D_3} \approx L_0 \mathbf{E}$. Then applying the Taylor series expansion to the term $\sqrt{1 - i\omega D_3}$, we have $\mathbf{v}_{w\_EM}\,(1 - i\omega D_3/2) \approx L_0 \mathbf{E}$. Now the r-component of $\mathbf{v}_{w\_EM}$ can be discretized as

$$\left(\frac{D_3}{2\Delta t} + \frac{1}{2} \right) v^{n+1/2}_{wr\_EM(j,k+1/2)} = \left(\frac{D_3}{2\Delta t} - \frac{1}{2} \right) v^{n-1/2}_{wr\_EM(j,k+1/2)} + L_0 E^n_{r(j,k+1/2)} \tag{58}$$

The discretization for the z-component can be represented similarly. In view of (58), the grid points of the electric field $\mathbf{E}$ and the relative flow velocity field $\mathbf{v}_w$ should be at the same locations (see the grid in Fig. 3). It is clear from (55) and (58) that by introducing the electric field to the FDTD algorithm of the acoustic logging simulation, the modified algorithm allows for the ES logging modeling. Now the converted acoustic wavefield in ES logging can be modeled if we know how to obtain the distribution of the electric field in the formation, which is the aim of the next section.

5. Finite-difference modeling of the electric field

The EM field in the interested region belongs to the near-field which is considered as a quasi-static field. This means that $\nabla \times \mathbf{E}(r,z) = 0$ throughout the modeled region, thus $\mathbf{E}(r,z) = -\nabla\varphi(r,z)$, where φ is the electric potential. Now we model by finite-difference method the distribution of the electric potential in the borehole and the formation.

The borehole fluid can be seen as a conductive medium, due to $\sigma_b/\omega\varepsilon_b \gg 1$ in this study, where σ_b and ε_b are the conductivity and the permittivity of the borehole fluid, respectively. Thus the electric potential satisfies the Poisson equation $\sigma_b\nabla^2\varphi = \nabla \cdot \mathbf{J}_0$ for the source region in the borehole, where $\mathbf{J}_0$ is the electric current density of the source. The vertical dipole point source along the borehole axis employed in this study is introduced by letting $\mathbf{J}_0 = P_e\delta(R)\mathbf{e}_z$, where P_e is the electric dipole moment, $\delta(R)$ is the Dirac delta function, R is the distance from the field point to the source, and $\mathbf{e}_z$ is the unit vector in the z-direction. We approximate the Dirac delta function by a distribution over a 5×5 grids area, so that $\delta(R) = 1/25\Delta r\Delta z$.

For the grid points out of the source region, the electric potential obeys the Laplace equation $\nabla^2\varphi = 0$. The discretization of the Poisson's equation and the Laplace's equation with respect to the electric potential in the cylindrical coordinates is formulated in Appendix A.

As the problem under consideration is unbounded in both the radial and axial directions, we put a boundary layer of an additional 50 grid points to all sides of the computational region to push the influence of the boundary far away from the computational region. Following Haines and Pride [29], we increase the step lengths of the grid points in the boundary layer by a factor of 1.3 from one grid point to the next, up to a maximum of 20 times the original step length. Outside the boundary layers, we employ Neumann condition $\partial\varphi/\partial m = 0$, where m is the direction normal to the boundary.

By the discretization of the electric potential at all the grid points, the equations $\mathbf{A}\Phi = d$ are established,where $\mathbf{A}$ is a sparse matrix that contains the coefficients of the electric potential in the discretized equations, and there are no more than five non-zero elements in each row of the matrix; Φ is an array that includes the unknown electric potential at all the grid points; d reflects the effects of the dipole source. These equations are solved by the conjugate-gradient iterative method. Thus we get the distribution of the electric potential in the borehole and formation at a given time and are able to model the converted acoustic wavefield by the processes described in Section 4.

6. Numerical modeling examples of the ES logging

In this section, we simulate the ES logging responses in a homogeneous fluid-saturated porous medium, and compare with those obtained from the analytical method [12]. The electric source pulse function is given by (42), which is identical with that for the acoustic logging simulation in this paper.

The electric field derived from the modeled electric potential according to $\mathbf{E}(r,z) = -\nabla\varphi(r,z)$, is compared with that obtained by the analytical method [12]. Comparisons of the electric field at different locations along the borehole wall are shown in Fig. 6. These results from the finite-difference method are modeled with the unit moment, i.e., $P_e = 1$, which corresponds to the peak value in the source pulse function given by (42) at the time of 0.250 ms. And those by the analytical method are the maximum values of the waveforms which arrive at 0.253 ms. The agreement shows the correctness of the finite-difference modeling of the electric field.

Fig. 7 shows the simulated waveforms of the converted pressure at different locations along the borehole axis in the ES logging. The waveforms are normalized with respect to the peak value at $z = 1$ m. It can be seen from Fig. 7 that there are four wave groups in the waveforms (shown by lines A–A, B–B, C–C and D–D, respectively) which are identical to those in [12], i.e., EM-accompanying wave group, compressional wave group, shear and pseudo-Rayleigh wave group, and Stoneley wave group. Fig. 8 shows the comparisons between the FDTD and the analytical methods of the waveforms in the ES logging. The EM-accompanying group is identical between the two methods, but the later three groups have small deviations both in amplitude and phase. The deviations are possibly resulted from the numerical approximations of the conjugate-gradient iterative method for solving the electric field in an unbounded region and caused by the approximate quantities introduced in the FDTD modeling of the acoustic logging. Despite of these deviations, the proposed numerical solution gives a very good approximation of the ES logging response.

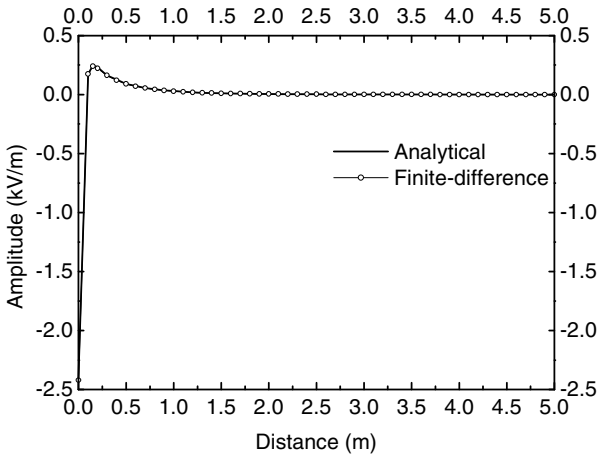

Fig. 6. Comparisons between the finite-difference and the analytical methods of the electric field at different locations along the borehole wall.

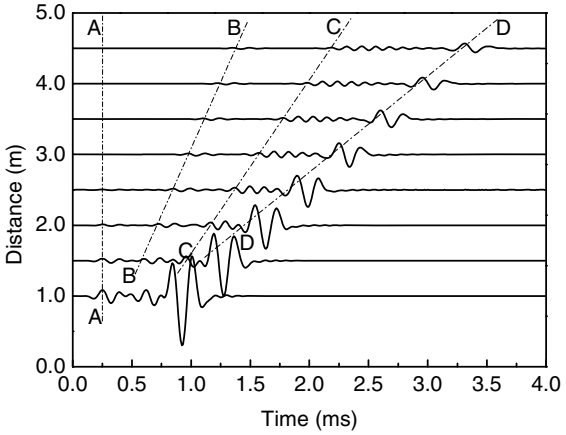

Fig. 7. Waveforms of the converted pressure in ES logging received at different locations along the borehole axis.

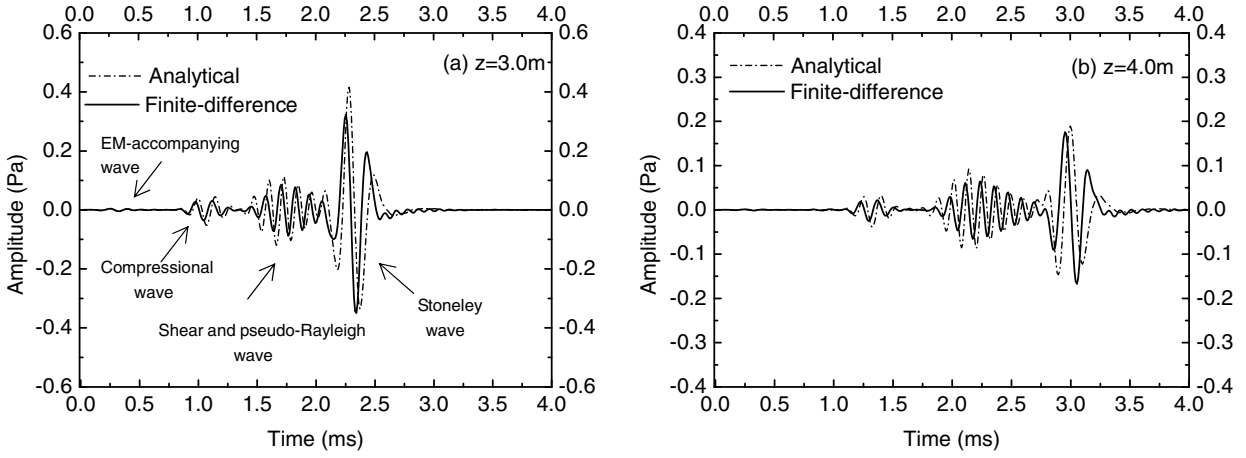

Fig. 8. Comparisons between the FDTD and the analytical methods of the waveforms of the converted pressure in ES logging. (a) $z = 3.0$ m. (b) $z = 4.0$ m.

7. Conclusions

We have proposed a FDTD scheme with nonsplitting PML for modeling the electroseismic as well as acoustic logging in a fluid-saturated porous formation. For the acoustic logging simulation, we introduced the dynamic permeability into the FDTD implementation to allow for both the inertial force dominated high-frequency domain and the low-frequency viscous flow domain of acoustic waves in porous media. This is advantageous over previous studies. Waveforms of the acoustic logging simulated by the FDTD algorithm agree with those obtained from the real-axis integration method.

By the finite-difference method we have simulated the quasi-static electric field excited by a vertical electric dipole along the borehole axis, and then compared the results with the analytical solutions. Agreement is observed between the finite-difference and the analytical results. The distributed electric field in the formation acts as the source of the converted acoustic wavefield in ES logging due to the electrokinetic effect. To simulate the ES logging, we modified the FDTD algorithm by replacing the acoustic monopole source of the acoustic logging with the distributed electric-field-driven source in the formation. We have compared the modeled waveforms with those obtained by the analytical method. The waveforms from the two different methods approximately agree.

The advantage of the finite-difference scheme over the analytical method is that it makes it possible modeling the ES logging responses in a horizontally stratified formation, which is more common in reality. We do not discuss this extension in this paper, but point out that it can be implemented by using the method of averaging the adjacent medium parameters to deal with the field quantities at the boundary between two layers. Moreover, the idea of finite-difference modeling of the ES logging in this paper can be applied for other ES conversion problems, such as vertical electroseismic profiling.

Acknowledgments

This work is supported by the National Natural Science Foundation of China (Grant No. 10272038) and the Special Research Funds of Seismology in China (Grant No. 2008419072).

Appendix A. Discretization of the equations with respect to the electric potential

By using the second-order central difference approximations, Poisson's equation $\sigma_b \nabla^2 \varphi = \nabla \cdot \mathbf{J}_0$ for the grid points in the source region is discretized as (see Fig. A.1),

$$A_0\varphi_0 = A_1\varphi_1 + A_2\varphi_2 + A_3\varphi_3 + A_4\varphi_4 - f_0, \tag{A.1}$$

where $f_0 = \nabla \cdot \mathbf{J}_0/\sigma_b = -P_e/25\Delta r\Delta z^2\sigma_b$, and

$$\begin{aligned} A_0 &= \frac{2}{h_2h_4} + \frac{1}{h_1h_3}\left(2 + \frac{h_3 - h_1}{r_0}\right), \\ A_1 &= \frac{1}{h_1(h_1 + h_3)}\left(2 + \frac{h_3}{r_0}\right), \\ A_2 &= \frac{2}{h_2(h_2 + h_4)}, \\ A_3 &= \frac{1}{h_3(h_1 + h_3)}\left(2 - \frac{h_1}{r_0}\right), \\ A_4 &= \frac{2}{h_4(h_2 + h_4)}, \end{aligned} \tag{A.2}$$

where r_0 is the distance from φ_0 to the z-axis, and h_n ($n = 1, 2, 3, 4$) are the step lengths, we set $h_1 = h_3 = \Delta r$ and $h_2 = h_4 = \Delta z$ for the grid points in the computational region. For the grid points out of the source region, f_0 becomes zero and (A.1) reduces to the discretized form of Laplace's equation $\nabla^2\varphi = 0$.

By applying the continuities of the electric potential and the electric current in the r-direction, the equation for the electric potential points at the borehole wall can be discretized as

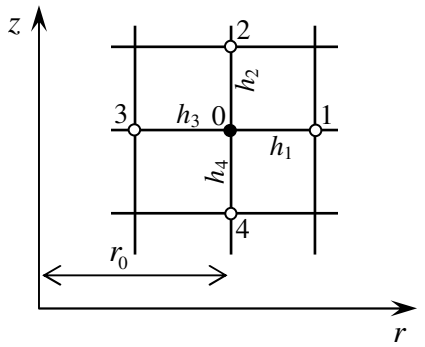

Fig. A.1. The grid for the finite-difference modeling of the electric potential φ.

$$A_0\left(1+\frac{A_1}{A_3}\frac{\sigma_0}{\sigma_b}\right)\varphi_0 = A_1\frac{\sigma_0}{\sigma_b}\left(1+\frac{A_1}{A_3}\right)\varphi_1 + A_2\left(1+\frac{A_1}{A_3}\frac{\sigma_0}{\sigma_b}\right)\varphi_2 + (A_1+A_3)\varphi_3 + A_4\left(1+\frac{A_1}{A_3}\frac{\sigma_0}{\sigma_b}\right)\varphi_4, \qquad (A.3)$$

where $\sigma_0 = \phi\sigma_f/\alpha_\infty$ is the low-frequency conductivity of the formation, and the approximation $\sigma \approx \sigma_0$ is reasonable for the frequency range in this study, σ_f is the conductivity of the porous fluid.

References

[1] S.R. Pride, Governing equations for the coupled electromagnetics and acoustics of porous media, Phys. Rev. B 50 (1994) 15678–15696.
[2] A.H. Thompson, G.A. Gist, Geophysical applications of electrokinetic conversion, Lead. Edge 12 (1993) 1169–1173.
[3] K.E. Butler, R.D. Russel, A.W. Kepic, M. Maxwell, Measurement of the seismoelectric response from a shallow boundary, Geophysics 61 (1996) 1769–1778.
[4] O.V. Mikhailov, M.W. Haartsen, M.N. Toksöz, Electroseimic investigation of the shallow subsurface: field measurements and numerical modeling, Geophysics 62 (1997) 97–105.
[5] A.H. Thompson, S.C. Hornbostel, J.S. Burns, T.J. Murray, R.A. Raschke, J.C. Wride, P.Z. McCammon, J.R. Sumner, G.H. Haake, M.S. Bixby, W.S. Ross, B.S. White, M. Zhou, P.K. Peczak, Field tests of electroseismic hydrocarbon detection, Geophysics 72 (2007) N1–N9.
[6] L. Jouniaux, J.-P. Pozzi, Determination of fluid flow variations at the Nankai Trough by electric and magnetic measurements in boreholes at the seafloor, J. Geophys. Res. 104 (1999) 29293–29309.
[7] S.R. Pride, F. Moreau, P. Gavrilenko, Mechanical and electrical response due to fluid-pressure equilibration following an earthquake, J. Geophys. Res. 109 (2004) B03302.
[8] Z. Zhu, M.W. Haartsen, M.N. Toksöz, Experimental studies of electrokinetic conversions in fluid-saturated borehole models, Geophysics 64 (1999) 1349–1356.
[9] Z. Zhu, M.N. Toksöz, Crosshole seismoelectric measurements in borehole models with fractures, Geophysics 68 (2003) 1519–1524.
[10] Z. Zhu, M.N. Toksöz, Seismoelectric and seismomagnetic measurements in fractured borehole models, Geophysics 70 (2005) F45–F51.
[11] H. Hu, J. Liu, Simulation of the converted electric field during acoustoelectric logging, in: 72nd Annual International Meeting Society of Exploration Geophysics, Expanded Abstracts 21, 2002, pp. 348–351.
[12] H. Hu, W. Guan, J.M. Harris, Theoretical simulation of electroacoustic borehole logging in a fluid-saturated porous formation, J. Acoust. Soc. Am. 122 (2007) 135–145.
[13] K.S. Yee, Numerical solution of initial boundary value problems involving Maxwell equations in isotropic media, IEEE Trans. Antenn. Propagat. 14 (1966) 302–307.
[14] A. Taflove, S.C. Hagness, Computational Electrodynamics: The Finite-Difference Time-Domain Method, third ed., Artech House, Norwood, MA, 2005.
[15] Y.H. Chen, W.C. Chew, M.L. Oristaglio, Application of perfectly matched layers to the transient modeling of subsurface EM problems, Geophysics 62 (1997) 1730–1736.
[16] F.L. Teixeira, W.C. Chew, M. Straka, M.L. Oristaglio, T. Wang, Finite-difference time-domain simulation of ground-penetrating radar on dispersive, inhomogeneous, and conductive soils, IEEE Trans. Geosci. Remote Sensing 36 (1998) 1928–1936.
[17] Q.H. Liu, J. Tao, The perfectly matched layer for acoustic waves in absorptive media, J. Acoust. Soc. Am. 102 (1997) 2072–2082.
[18] Y.Q. Zeng, J.Q. He, Q.H. Liu, The application of the PML in numerical modeling of wave propagation in poroelastic media, Geophysics 66 (2001) 1258–1266.
[19] T. Wang, X.M. Tang, Finite-difference modeling of elastic wave propagation: a nonsplitting perfectly matched layer approach, Geophysics 68 (2003) 1749–1755.

[20] M.A. Biot, Theory of propagation of elastic waves in a fluid-saturated porous solid. I. Low-frequency range, J. Acoust. Soc. Am. 28 (1956) 168–178.
[21] M.A. Biot, Mechanics of deformation and acoustic propagation in porous media, J. Appl. Phys. 33 (1962) 1482–1498.
[22] D.L. Johnson, J. Koplik, R. Dashen, Theory of dynamic permeability and tortuosity in fluid-saturated porous media, J. Fluid Mech. 176 (1987) 379–402.
[23] J.P. Bérenger, A perfectly matched layer for the absorption of electromagnetic waves, J. Comput. Phys. 114 (1994) 185–200.
[24] J.P. Bérenger, Three-dimensional perfectly matched layer for the absorption of electromagnetic waves, J. Comput. Phys. (1996) 363–379.
[25] W.C. Chew, Q.H. Liu, Perfectly matched layers for elastodynamics: a new absorbing boundary condition, J. Comput. Acoust. 4 (1996) 341–359.
[26] J.A. Roden, S.D. Gedney, Convolution PML (CPML): an efficient FDTD implementation of the CFS-PML for arbitrary media, Microwave Opt. Technol. Lett. 27 (2000) 334–339.
[27] J.H. Rosenbaum, Synthetic microseismograms: logging in porous formations, Geophysics 39 (1974) 14–32.
[28] B.S. White, Asymptotic theory of electroseismic prospecting, SIAM J. Appl. Math. 65 (2005) 1443–1462.
[29] S.S. Haines, S.R. Pride, Seismoelectric numerical modeling on a grid, Geophysics 71 (2006) N57–N65.
[30] C.J. Randall, D.J. Scheibner, P.T. Wu, Multipole borehole acoustic waveforms: synthetic logs with beds and borehole washouts, Geophysics 56 (1991) 1757–1769.
[31] L. Tsang, D. Rader, Numerical evaluation of the transient acoustic waveform due to a point source in a fluid-filled borehole, Geophysics 44 (1979) 1706–1720.
[32] R.M. Alford, K.R. Kelly, D.M. Boore, Accuracy of finite-difference modeling of the acoustic wave equation, Geophysics 39 (1974) 834–842.
[33] L. Vernik, Predicting lithology and transport properties from acoustic velocities based on petrophysical classification of siliclastics, Geophysics 59 (1994) 420–427.